

# Computer Methods in Biomechanics and Biomedical Engineering

ISSN: (Print) (Online) Journal homepage: <https://www.tandfonline.com/loi/gcmb20>

## Overset meshing in combination with novel blended weak-strong fluid-structure interactions for simulations of a translating valve in series with a second valve

J. Bornoff, H.S. Gill, A. Najar, I.L. Perkins, A.N. Cookson & K.H. Fraser

To cite this article: J. Bornoff, H.S. Gill, A. Najar, I.L. Perkins, A.N. Cookson & K.H. Fraser (2023): Overset meshing in combination with novel blended weak-strong fluid-structure interactions for simulations of a translating valve in series with a second valve, Computer Methods in Biomechanics and Biomedical Engineering, DOI: [10.1080/10255842.2023.2199903](https://doi.org/10.1080/10255842.2023.2199903)

To link to this article: <https://doi.org/10.1080/10255842.2023.2199903>



© 2023 The Author(s). Published by Informa UK Limited, trading as Taylor & Francis Group



[View supplementary material](#)



Published online: 18 Apr 2023.



[Submit your article to this journal](#)



[View related articles](#)



[View Crossmark data](#)

# Overset meshing in combination with novel blended weak-strong fluid-structure interactions for simulations of a translating valve in series with a second valve

J. Bornoff<sup>a</sup>, H.S. Gill<sup>a,b</sup>, A. Najar<sup>c</sup>, I.L. Perkins<sup>c</sup>, A.N. Cookson<sup>a,b</sup> and K.H. Fraser<sup>a,b</sup>

<sup>a</sup>Department of Mechanical Engineering, University of Bath, Bath, UK; <sup>b</sup>Centre for Therapeutic Innovation, University of Bath, Bath, UK; <sup>c</sup>Scandinavian Real Heart AB, Västerås, Västmanland, Sweden

## ABSTRACT

Mechanical circulatory support (MCS) devices can bridge the gap to transplant whilst awaiting a viable donor heart. The Realheart Total Artificial Heart is a novel positive-displacement MCS that generates pulsatile flow *via* bileaflet mechanical valves. This study developed a combined computational fluid dynamics and fluid-structure interaction (FSI) methodology for simulating positive displacement bileaflet valves. Overset meshing discretised the fluid domain, and a blended weak-strong coupling FSI algorithm was combined with variable time-stepping. Four operating conditions of relevant stroke lengths and rates were assessed. The results demonstrated this modelling strategy is stable and efficient for modelling positive-displacement artificial hearts.

## ARTICLE HISTORY

Received 1 June 2022  
Accepted 30 March 2023

## KEYWORDS

Computational fluid dynamics; fluid-structure interactions; mechanical heart valve; positive displacement; total artificial heart

## 1. Introduction


Heart failure (HF) currently affects 64.35 million patients worldwide (Lippi and Sanchis-Gomar 2020). Treatments for HF range from healthy lifestyle changes and medication to heart transplant surgery, which is considered the gold standard in treating end-stage HF. However, the number of available donors is limited. Since 2011, the number of patients on the heart transplant waiting list in the UK has increased by 85%, but there are only half the number of donors available (NHS BaT 2021). To alleviate the shortfall, doctors can turn to mechanical circulatory support devices to bridge the gap to transplant. These devices include ventricular assist devices, used in cases of ventricular failure to partially assist in cardiac function, and total artificial hearts (TAHs), which fully replace the native heart in cases of biventricular HF.

The Syncardia (Tucson, AZ, USA) TAH, a pneumatically driven pulsatile TAH (Slepian et al. 2013), is currently the only FDA-approved bridge-to-transplant TAH (Melton et al. 2019). However, it suffers from complications including infection and thromboembolic events (Torregrossa et al. 2014) that newer TAHs are

seeking to overcome. The CARMAT (Paris, France) Aeson TAH, a positive-displacement device that aims to improve biocompatibility by using bioprosthetic materials and mimicking the shape of the heart (Mohacsi and Leprince 2014), has recently been granted the CE mark in Europe and has gained approval for early US feasibility studies (Han 2021).

The Realheart TAH, developed by Scandinavian Real Heart (Västerås, Sweden), is a novel TAH that aims to improve biocompatibility by mimicking a key component of the mechanics of the native heart: the vertical translation of an atrioventricular (AV) plane (Szabo et al. 2018). When the native heart contracts during systole, the vertical displacement of the base of the ventricle towards the apex accounts for 60% of the stroke volume (Carlsson et al. 2007). The Realheart TAH employs this positive-displacement pumping mechanism to generate pulsatile blood flow, using a pair of bileaflet mechanical heart valves (BMHVs) in the atrioventricular and semi-lunar positions to govern the forward motion of blood through the device. As such the BMHVs are a key component of the TAH and understanding their motion is vital to predicting fluid flow and pressure characteristics. Mechanical heart valves (MHVs) have been associated

CONTACT K.H. Fraser  [K.H.Fraser@bath.ac.uk](mailto:K.H.Fraser@bath.ac.uk)

 Supplemental data for this article can be accessed online at <https://doi.org/10.1080/10255842.2023.2199903>.

© 2023 The Author(s). Published by Informa UK Limited, trading as Taylor & Francis Group  
This is an Open Access article distributed under the terms of the Creative Commons Attribution License (<http://creativecommons.org/licenses/by/4.0/>), which permits unrestricted use, distribution, and reproduction in any medium, provided the original work is properly cited. The terms on which this article has been published allow the posting of the Accepted Manuscript in a repository by the author(s) or with their consent.

with complications such as haemolysis and coagulation due to non-physiological flow patterns that are generated (Dasi et al. 2009) and therefore knowledge of shear stresses and exposure times around the valves are also required.

Computational fluid dynamics (CFD) has been widely used to simulate blood flow through MHVs to gain an insight into these problems. Simulating the interaction between MHVs and the blood is a fluid-structure interaction (FSI) problem and can be solved using different numerical techniques including: the arbitrary Lagrangian-Eulerian (ALE) or moving grid method, the immersed boundary (IB) or fixed grid method, and the overlapping domain (OD) method, known as overset or chimera meshing. The ALE method is the most common FSI technique, as it is widely available and in theory more accurate for near wall modelling when compared to the IB method, as the ALE method explicitly captures the fluid-solid interface (Bavo et al. 2016). However, recent high-order IB methods that implement sharp interfaces between the fluid and solid result in improved shear stress capture (Kolahdouz et al. 2021). IB methods have been developed with large displacements and elastodynamic behaviour of structures in mind (Tian et al. 2014; Nestola et al. 2019) and have been applied to bioprosthetic and trileaflet prosthetic heart valves (Hsu et al. 2015, Borazjani 2013, Gilmanov et al. 2015) as well as bicuspid aortic valves (Gilmanov and Sotiropoulos 2016). Early approaches of the ALE method simulated 2D leaflet sections (Dumont et al. 2004), but as computational power improved, the models were extended to full 3D MHVs in realistic aortic geometries (Nobili et al. 2008; Mirkhani et al. 2016). The IB method can handle large solid displacements efficiently for MHV FSI problems (Borazjani et al. 2010), as well as providing improved stability over the ALE method as mesh motion and deformation are not required (Bavo et al. 2016). The OD method features less frequently for MHV applications, possibly due to a lack of commercial software support until recently. It offers accuracy, like the ALE method, without the need for mesh deformation, like the IB method (Spühler and Hoffman 2021). Compared to the ALE approach, the OD method also simplifies mesh generation of more complex devices such as a TAH, where each component can be individually meshed and combined. This approach also allows for new components to be included or other parts suppressed with ease, whilst also allowing for the swapping of parts to analyse geometry variations, all without the need for a complete regeneration of the

mesh. The OD approach has been used to obtain flow structures in a fully open valve configurations (Ge et al. 2003), as well as prescribed motion valves in an anatomically accurate human aorta (Nowak et al. 2020). Nowak et al. (2020), concluded the OD method was stable and efficient, and produced typical BMHV fluid flow phenomena.

FSI methods have also been applied to full device simulations. Luraghi et al. (2018) investigated the CARMAT TAH using a combined IB and ALE approach. The initial IB approach determined valve and membrane displacement, which was then used as prescribed motion in a subsequent ALE study to determine local velocity fields and shear stresses. Al-Azawy et al. (2016) used the OD method to model an LVAD with prescribed motion of the monoleaflet valves and pusher plate, and returned good agreement with experimental data.

For the Realheart TAH, Kelly et al. (2022) investigated four computational methods for the AV plane and valve motion using an IB approach. These were: prescribed idealised motion; prescribed motion using motion data obtained through video capture of the valves *in vitro*; prescribed motion of the mitral valve but fluid-driven motion of the aortic valve; and fluid-driven motion of both valves. The motion prescribed from video analysis of experiments returned the most accurate solution, whilst the fluid-driven approach could not account for the instabilities of the complex valve motion. However, the video data approach was restrictive as the range of *in silico* studies was limited by the experimental analysis available. Additionally, the IB approach resulted in poor shear stress resolution on the leaflet surface – an area of great interest with regards to blood damage.

This study sought to produce a new modelling approach for the motion of positive-displacement MHVs, by creating a fluid-driven strategy which would eliminate the need for prior experimental data and provide accurate shear stress capture in the vicinity of the valve leaflets. The modelling strategy was developed and tested on a simplified positive-displacement pump geometry and the valve kinematics, fluid flow characteristics and shear stresses were analysed to assess model stability and accuracy. The modelling strategy can be readily transferred to the Realheart TAH, as well as other positive-displacement artificial hearts with MHVs.

## 2. Methods

### 2.1. Computational domain

To accelerate development of the modelling approach, a simplified positive displacement pump embodying

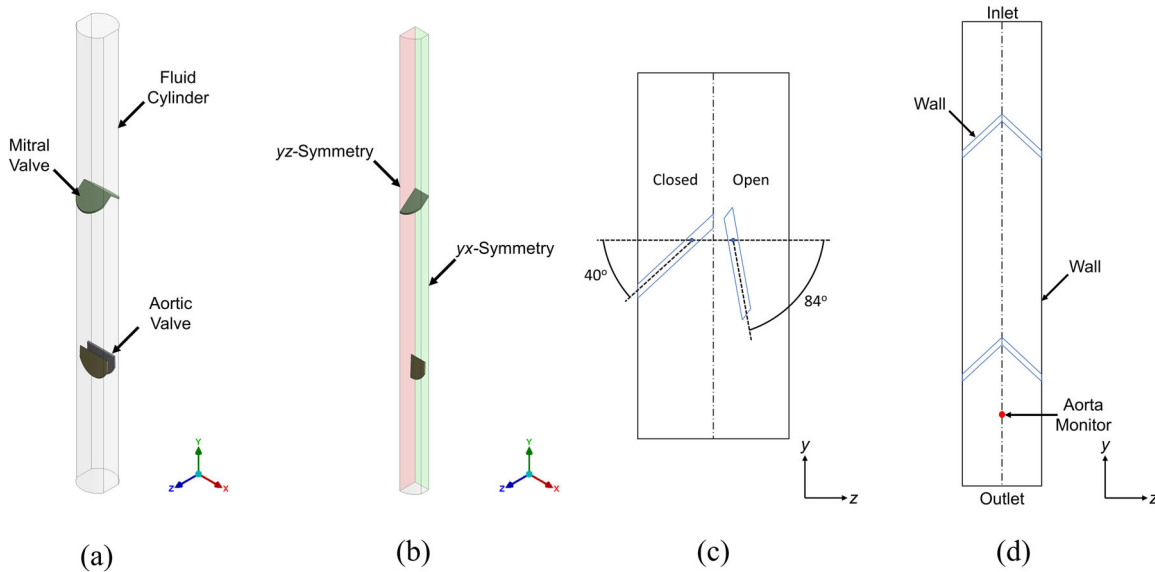


**Figure 1.** Outline of the computational domain (a) Full domain geometry with fluid cylinder and two BMHVs (b) 1/4 domain geometry: yz-symmetry (red), yx-symmetry (green) (c) Angle of leaflet in closed and open positions (d) Monitor point location with inlet, outlet, and wall boundaries.

the critical features of the Realheart TAH was used. The computational domain consisted of a 3D fluid cylinder containing two BMHVs based on the On-X valve, aligned in series, shown in Figure 1(a), and was generated using Ansys DesignModeler V2021.R1 (ANSYS Inc., Canonsburg, PA, USA). The model had two degrees of symmetry, in the yz and yx planes, and as such a quarter model was considered, shown in Figure 1(b).

The two valves represented the mitral (upstream) and aortic (downstream) valves. The valve leaflets were positioned at 40° to the horizontal when closed and 84° to the horizontal when fully open, shown in Figure 1(c), similar to Mirkhani et al. (2016). The motion behaviour of the valves, which was the same as the full Realheart TAH, was as follows: the mitral valve underwent a forced vertical sinusoidal translation, approximating the translation of the AV plane. As the mitral valve travelled upwards, a pressure gradient across the valve leaflets caused the mitral valve to open. When the mitral valve travelled downwards, a pressure gradient was created in the opposite direction and the mitral valve leaflets closed. This then increased the pressure between the valves and opened the aortic valve. The valve leaflets of both the aortic and mitral valves could open and close freely due to the fluid-structure interaction, whilst the sinusoidal translation of the mitral valve was prescribed at the pivot point.

Two key simplifications were made that improved computational efficiency – the valve housing was not

explicitly modelled, and the peripheral gap around the outside of the leaflet, as well as between the leaflets, was not considered. Instead, the cross section of the fluid cylinder was the same shape as the valve leaflets in the fully closed position. This approximated a perfect seal between the valve leaflets and fluid cylinder when the valves were fully closed. This removed the need for regions of high cell density around the leaflet edges to explicitly model the gaps, reducing the overall cell count and improving model efficiency.

A monitor point was placed downstream of the aortic valve, representing the aorta, to measure pressure variation, shown in Figure 1(d).

## 2.2. Boundary conditions

The left side of the Realheart TAH was used as a reference for boundary condition values. At the outlet, a two-element Windkessel model approximated the haemodynamic pressure response of the downstream vasculature: resistance  $R = 3e8 \text{ kg m}^{-4} \text{ s}^{-1}$  and compliance  $C = 1e-10 \text{ m}^4 \text{ s}^2 \text{ kg}^{-1}$ . The value of  $R$  was chosen to generate a peak systolic pressure of 120 mmHg and  $C$  was then varied to produce a smoothed pressure response. The inlet was assigned a constant pressure of 15 mmHg approximating pulmonary venous pressure (Kelly et al. 2022). Symmetry conditions were applied to the two symmetry faces, and no-slip walls were used on the remaining outer surfaces of the fluid cylinder, as well as the surfaces of the leaflets.

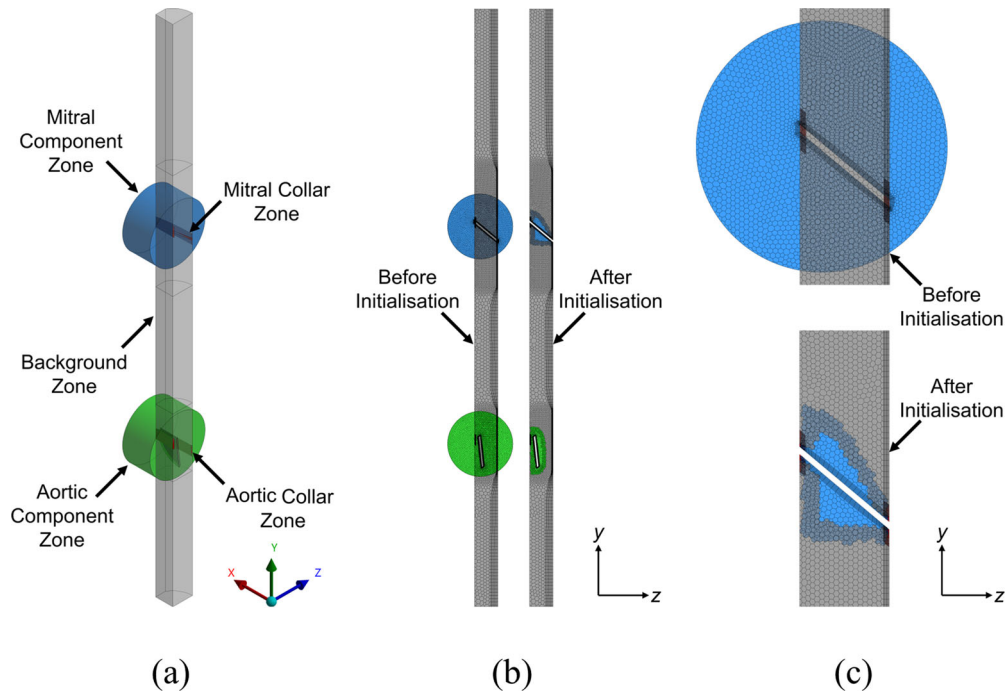


**Figure 2.** Fluid mesh definition (a) Fluid mesh zones: mitral component zone (blue), aortic component zone (green), background zone (grey), collar zones (red) (b) before and after initialisation of whole mesh (c) before and after initialisation of mitral mesh zone.

**Table 1.** Mesh densities of the three meshes used in the mesh convergence study.

	Mesh Density	Tetrahedral Element Count	Polyhedral Element Count
1	Coarse	0.84M	0.28M
2	Medium	1.2M	0.4M
3	Fine	2.1M	0.7M

### 2.3. Meshing

Overset meshing was used to incorporate the BMHVs into the fluid cylinder. The overset meshing approach maintained a consistent and refined mesh around the surface of the valve leaflets, enabling accurate shear stress capture. Five fluid mesh zones were generated: the background zone for the fluid cylinder, two component zones for the mitral and aortic valves, and two component collar meshes, shown in Figure 2(a). Due to some differences in mesh resolution between the background mesh and leaflet meshes, collar meshes were included to improve the resolution of the contact between the outer faces of the valve leaflets and the background walls and symmetry faces.

The background zone mesh was split into coarse and fine element regions of 2 mm and 0.75 mm element size respectively and joined together with conformal interfaces. The fine regions overlapped with the valve component zones, which had a body element sizing of 0.75 mm and face sizing of 0.35 mm on all valve leaflet surfaces. Prism layers were used on all

walls and the leaflet surfaces to capture boundary layers. Upon initialisation of the solution, the separate mesh zones combined to form a single continuous mesh, shown in Figure 2(b) and (c).

Initial meshes were generated using Ansys Meshing V2021.R1 (Ansys Inc.). The collar zones were meshed with hexahedral elements. The background zone and valve component zones were meshed with tetrahedral elements, which were later converted to polyhedral elements within Ansys Fluent V2021.R1 (Ansys Inc.), reducing the total cell count by a factor of approximately 3x.

The mesh convergence study used three different meshes of increasing element counts, shown in Table 1. Each mesh was solved for two cycles, and the valve kinematics and wall shear stresses were monitored. The focal point of mesh refinement was in the immediate region around the valve leaflet, where the leaflet face element size, valve component zone body size, the fine mesh body size of the background zone and collar component zone body size were varied to produce the three meshes.

### 2.4. Valve motion

Motion of the valves was achieved through the dynamic mesh utility and intrinsic six-degrees of freedom (6DoF) solver within Ansys Fluent. Pre-existing User Defined Functions (UDFs) were adapted and

used to assign the motion properties to each of the moving zones.

The *Define\_CG\_Motion* UDF was used for the vertical translation of the mitral valve pivot, denoted as the AV plane, by assigning a sinusoidal  $y$  velocity to the mitral component zone (Figure 2(a)) with Equation (1),

$$v_y = -Afcos(ft) \quad (1)$$

where  $A$  (mm) was the amplitude, or half the stroke length of the translation,  $f$  (rad  $s^{-1}$ ) was the frequency or stroke rate (bpm) of the translation, and  $t$  (s) was the time. Four studies were undertaken at  $A = 12.5, 25$  mm (equivalent to a stroke length of 25 mm and 50 mm) and  $f = 80, 100$  bpm, and the response of the model to these parameters was measured.

The *Define\_SDOF\_Properties* UDF was employed to achieve fluid-driven rotation of the valve leaflets. For the valve leaflets, the motion was constrained to rotate around the  $x$  axis at the valve pivot point. Contact between leaflets was not explicitly modelled, instead the motion was constrained by including limits on the angle of rotation,  $\theta$  ( $^\circ$ ), between  $40^\circ$  (fully closed) and  $84^\circ$  (fully opened). The rotation of the valve leaflets was calculated by the 6DoF solver. The mass of each leaflet was  $m = 0.35$  g, and the moment of inertia  $I = 2.3e-8$  kg  $m^2$ .

## 2.5. Numerical procedure

Ansys Fluent was used to solve the Navier-Stokes and 6DoF equations. The solution strategy used an angle-dependent blend of weak and strong coupling algorithms between the fluid flow and structural domain (Figure 3). Strong coupling, where the position of the valve leaflets was updated at the end of every iteration, was used to maximise stability and accuracy of the solution. Weak coupling, where the position of the valve leaflets was updated at the end of every time step, was used to maximise computational efficiency. With this blended approach, it was possible to choose which phases of valve motion were strongly and weakly coupled depending on threshold valve leaflet angles, thus achieving a balance between stability, accuracy and efficiency. In this study, the focus was minimising computation time, whilst still maintaining a minimum level of solution stability. This was achieved by only using strong coupling when one valve closed and the other opened, activating when valve angles were less than  $7^\circ$  (scheme denoted as B1). Additionally, a scheme which utilised strong coupling for both small ( $<7^\circ$ ) and large ( $37^\circ - 44^\circ$ ) valve angles was also considered (denoted as B2), the larger

threshold related to leaflet rebound and flutter, and both schemes were compared to a fully strongly (denoted as FS) coupled solution at a stroke rate of 80 bpm and stroke length of 25 mm.

No turbulence model was used, as the peak bulk flow Reynolds number (Re) was 900, well below the threshold for turbulence in a pipe (Darbyshire and Mullin 1995).

The coupled algorithm was used to solve the Navier-Stokes equations, using a second-order pressure discretisation scheme and a second-order upwind scheme for the momentum. A least-squares cell based gradient scheme was used throughout. A first order pressure interpolation scheme using a least-squares method was used at overset interfaces. Solution relaxation was used for both the pressure and momentum variables, as well as for higher order terms, to improve convergence behaviour and reduce the risk of solution divergence. The default value of 0.75 was used for these relaxation parameters.

The model was initialised with the mitral valve at  $y = 0$  mm and moving downwards with a velocity  $v_y = -Af$  m  $s^{-1}$  (eq. (1) with  $t = 0$  s). The aortic valve was in a fully open state so that there was no large displacement of the aortic valve at the beginning of the solution. This allowed the fluid flow solution to converge faster during this time, reducing computational cost. The fluid was initialised in a quiescent state, with a uniform pressure of 90 mmHg. The outlet Windkessel model was also initialised at 90 mmHg so that there was no initial pressure jump across the outlet interface. Fluid properties were density  $\rho = 1060$  kg  $m^{-3}$ , and fixed viscosity  $\mu = 0.0035$  N  $m^{-1} s^{-2}$ , approximating blood as a Newtonian fluid.

A first-order implicit transient formulation scheme was used, as the second-order scheme was not compatible with overset meshing. A custom angle-dependent variable time stepping scheme was developed and implemented to improve accuracy and stability where needed, whilst improving computational efficiency. The scheme was divided into two main conditions, outlined in Table 2. A maximum  $dt$  of 2.5 ms was used as solution instabilities were experienced with larger values.

All simulations were performed in parallel on an Intel Xeon workstation with 4 cores at 3.50 GHz and 128 GB of memory.

## 3. Results

All results shown use the small angle blended scheme (B1), except for the 'Blended Weak Strong Coupling' section which compares two blended schemes with a fully strongly coupled scheme.

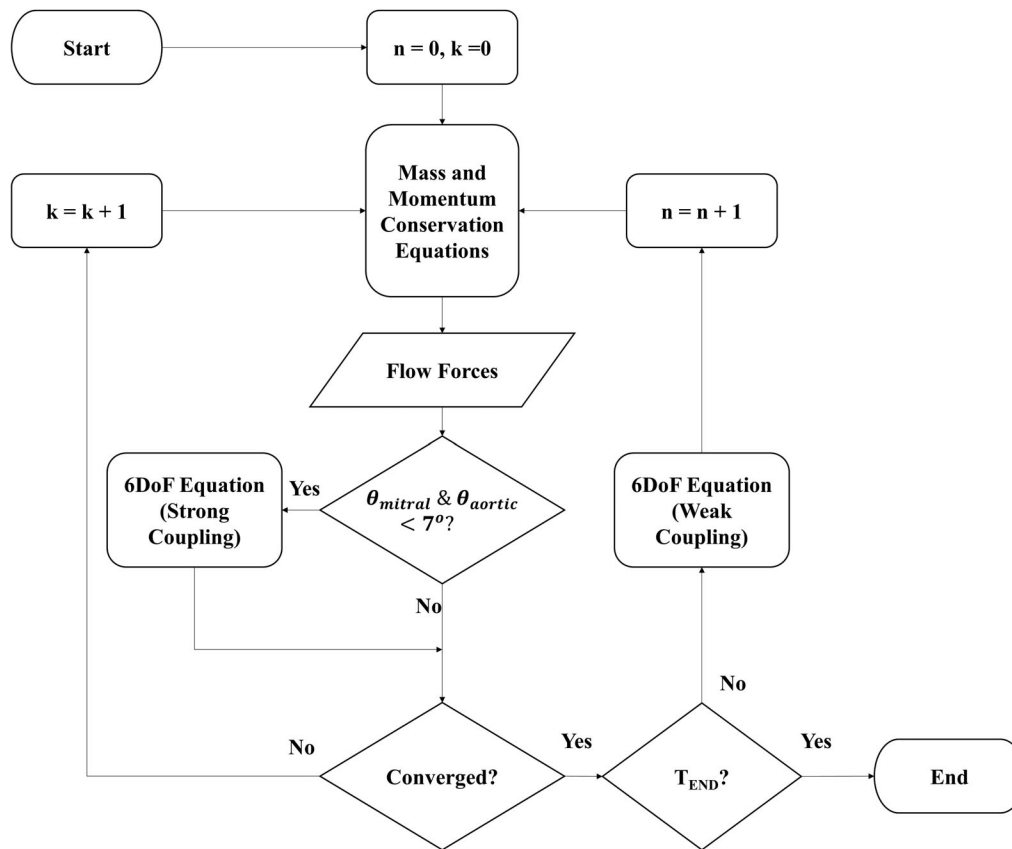


**Figure 3.** Solution strategy flow diagram. Rectangular boxes represent processes, diamond boxes represent decisions, parallelograms represent input/output. Arrows are the flow of logic through the strategy.  $n$  is the time step number,  $k$  is the iteration number, and  $T_{END}$  is the end time of the solution.

### 3.1. Mesh study

The three meshes were compared using the leaflet angle and area average wall shear stress ( $\overline{WSS}$ ) of the mitral and aortic valve leaflets over the course of two cycles at a stroke length of 25 mm and stroke rate of 100 bpm.

The mitral and aortic valves in the fine and medium meshes opened and closed at similar times, but the valves in the coarse mesh opened at slightly different times (Figure 4). The profile of the mitral and aortic valve  $\overline{WSS}$  was similar for both the fine and medium meshes, whilst the coarse mesh  $\overline{WSS}$  for both valves reflected the differences in the opening and closing times (Figure 5). Peak mitral valve  $\overline{WSS}$  decreased for an increase in mesh density, whilst peak aortic valve  $\overline{WSS}$  increased for an increase in mesh density. The root mean square error (RMSE) between the medium and fine mesh was  $2.0^\circ$  (4.6% of the peak value) and  $2.9^\circ$  (6.6% of the peak value) for the mitral and aortic valve leaflet angles respectively, and 4.3 Pa (9% of the peak value) and 8.5 Pa (6.8% of the peak value) for the mitral and aortic valve  $\overline{WSS}$  respectively. In all cases the coarse mesh returned greater RMSE values. The total CPU hours for the medium and fine meshes was 192 and 360 respectively. Therefore, the

medium mesh was used for the study as it balanced computational time and accuracy.

### 3.2. Variable time stepping

The change in  $\theta_{mitral}$  and  $\theta_{aortic}$  varied linearly with  $dt$  size, limited to  $0.5^\circ/dt$  above  $2^\circ$  and  $0.1^\circ/dt$  below  $2^\circ$  (Figure 6). The maximum  $dt$  of 2.5 ms occurred when both valves were not moving, or when the change in angle per time step for either valve was less than  $0.5^\circ/dt$ , as seen between the 300<sup>th</sup> and 350<sup>th</sup> time step. Compared to a fixed  $dt$  scheme of 50,000-time steps for four cycles, the variable  $dt$  scheme required 2,100-time steps to complete the four cycles, a reduction of 96%.

### 3.3. Flow distribution

Time dependant velocity fields for the four cases tested are shown *via* videos in the [supplementary files](#). The distribution of the fluid velocity was investigated over the last cycle, at time points corresponding to both valves fully open ( $\theta = 44^\circ$ ) (Figure 7).

### 3.4. Leaflet kinematics

$\theta_{mitral}$  and  $\theta_{aortic}$  was captured for each operating condition and is shown alongside the sinusoidal displacement of the AV plane (Figure 8). The opening of one valve and the closing of another, and vice versa, occurred at the same time step. Mitral valve closure and aortic valve opening happened when the AV plane was translating downwards, whilst mitral valve opening and aortic valve closing occurred when the AV plane was translating upwards.

There was an increase in  $\omega_{opening}$  for both the mitral and aortic valve for an increase in stroke rate and stroke length (Figure 9). However,  $\omega_{closing}$  only increased for both valves with an increase in stroke length but did not increase with an increase in stroke rate.

### 3.5. Pressure variation

The variation in pressure in the aortic section was measured over time to assess the effect of the two-element Windkessel at the outlet (Figure 10). When the aortic valve was closed (before approximately cycle number = 1.9), the aortic pressure was a constant 90 mmHg for all cases. When the aortic valve opened, the pressure in the aorta increased as the flow rate through the outlet also increased, where the peak aortic pressure occurred at the peak outlet flow rate. The peak aortic pressure increased with an increase in stroke length and stroke rate; stroke length had the largest influence. When the flow began reversing, the pressure in the aorta dropped below the outlet operating pressure of 90 mmHg, until the aortic pressure reached its minimum as the aortic valve closed. The minimum aortic pressure at this time decreased with an increase in stroke length, however there was little difference when varying stroke rate. After aortic valve closure, the aortic pressure in all four cases returned to the operating pressure due to the compliance element of the Windkessel.

### 3.6. Shear stress

Peaks in both  $\overline{WSS}_{mitral}$  and  $\overline{WSS}_{aortic}$  occurred at instantaneous valve opening and closing; the magnitude of the peak was generally greater for valve opening

(Figure 11). Time-averaged  $\overline{WSS}$  ( $\overline{TAWSS}$ ) was calculated for each valve leaflet and is shown in Table 3, where  $\overline{TAWSS}$  increased for both valves for an increase in stroke rate and stroke length. The distribution of wall shear stress over the valve leaflet surfaces when the valves were fully open shows the largest values are along the leading edges (Figure 12).

### 3.7. Volume flow rate

The volume flow rate,  $Q$  ( $L \min^{-1}$ ), was measured through the inlet,  $Q_{inlet}$  (Figure 13(a)). Forward flow is indicated by positive volume flow rate and backflow is negative. An increase in stroke rate and stroke length both returned an increase in peak  $Q_{inlet}$ . The cumulative output fluid volume,  $V$  (mL), defined as the fluid moved forward through the domain less the backward fluid flow, was calculated (Figure 13(b)).  $V$  increased for an increase in stroke length, however after four cycles,

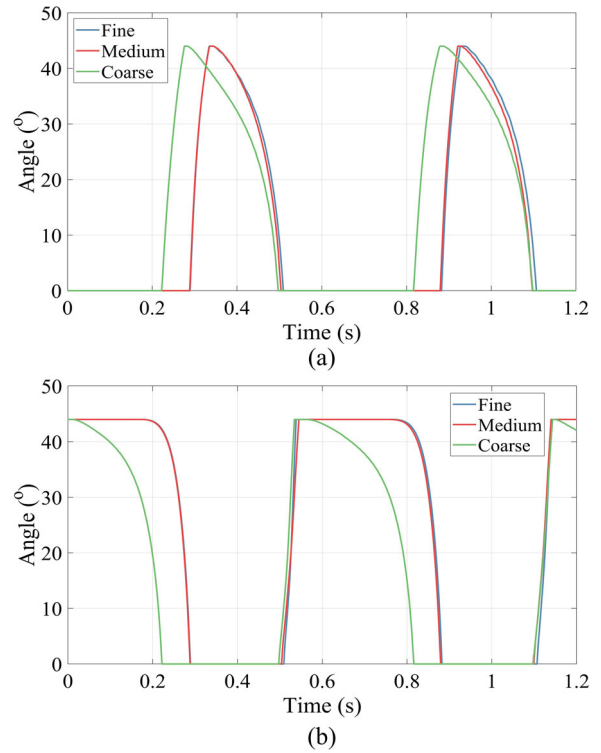
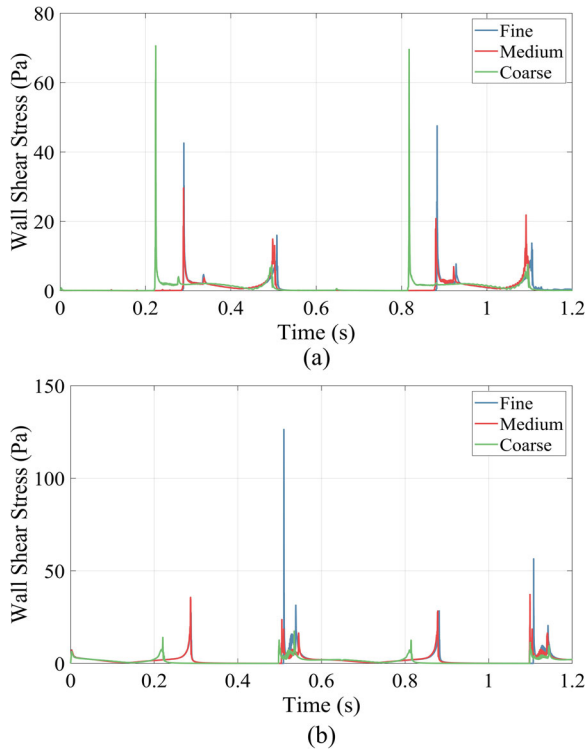


Figure 4. Variation in  $\theta$  over time for the coarse, medium, and fine meshes for the (a) mitral and (b) aortic valves.

Table 2. Variable time stepping scheme conditions. Two conditions depend on moving and stationary valves. When valves are moving, two sub conditions interrogate the leaflet angle, and adjust the time step accordingly.

Number	Condition	Condition	Timestep Size
1 (Moving)	$ \omega_{mitral}  > 0$ or $ \omega_{aortic}  > 0$	$\theta_{mitral} > 2^\circ$ or $\theta_{aortic} > 2^\circ$ $\theta_{mitral} < 2^\circ$ and $\theta_{aortic} < 2^\circ$	$dt = \min\left(\frac{0.5^\circ}{\omega_{mitral}}, \frac{0.5^\circ}{\omega_{aortic}}, 2.5 \text{ ms}\right)$ $dt = \min\left(\frac{0.1^\circ}{\omega_{mitral}}, \frac{0.1^\circ}{\omega_{aortic}}\right)$
2 (Stationary)	$\omega_{mitral} = 0$ and $\omega_{aortic} = 0$		$dt = 2.5 \text{ ms}$





**Figure 5.** Variation in  $\overline{WSS}$  over time for the coarse, medium and fine meshes for the (a) mitral and (b) aortic valves.

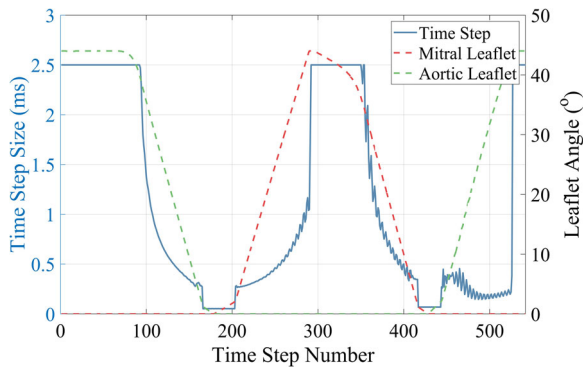


**Figure 6.** Variability in time step size and  $\theta$  for the mitral and aortic valves, showing the effect of the variable time stepping scheme outlined in Table 2.

there was little difference in  $V$  with an increase in stroke rate.

Comparing the forward and backward fluid volumes ( $V_{forward}$  and  $V_{backward}$ ) in Figure 14(a),  $V_{forward}$  increased for an increase in stroke length but decreased for an increase in stroke rate.  $V_{backward}$  decreased with both an increase in stroke rate and stroke length. Peak volume flow rate,  $Q_{peak}$  ( $L \min^{-1}$ ), increased with an increase in stroke rate and stroke length (Figure 14(b)). The change in average flow rate,  $Q_{average}$  ( $L \min^{-1}$ ), was marginal for a change in stroke rate, but a doubling in stroke length increased  $Q_{average}$  by a factor of approximately three.

### 3.8. Blended weak strong coupling

A fully strongly (FS) coupled solve was compared to the two blended schemes to assess any loss of solution accuracy when using a blended approach. The first blended scheme (B1) considered small ( $<7^\circ$ ) valve angles, whilst the second scheme (B2) considered both small ( $<7^\circ$ ) and large ( $37^\circ - 44^\circ$ ) valve angles.

Largest differences in mitral valve angle were observed during valve closure, where B1 closed 0.016s before B2, and 0.024s before FS (Figure 15(a)). The aortic valve reached fully open in B1 first, 0.032s before B2 and 0.061s before FS (Figure 15(b)). Timings of peak  $\overline{WSS}$  occurred at the same time as valve opening and closing of the three schemes. FS returned a smoother  $\overline{WSS}$  profile for both valves during valve opening, with both B1 and B2 displaying small oscillations (Figure 15(c) and (d)).

The RMSE between B1 and FS was  $8.6^\circ$  and  $11.3^\circ$  (19.5% and 25.7% of the maximum value) for the mitral and aortic valve leaflet angles respectively, and 2.9 Pa and 4.3 Pa (13.4% and 16.4% of the maximum value) for the mitral and aortic valve leaflet  $\overline{WSS}$  respectively. Between B2 and FS, the RMSE was  $3.6^\circ$  and  $3.9^\circ$  (8.1% and 8.8% of the maximum value) for the leaflet angles, and 4.7 Pa and 5.3 Pa (11.2% and 8.9% of the maximum value) for the leaflet  $\overline{WSS}$ . The total number of CPU hours for one cycle was 96, 144 and 192 for B1, B2 and FS respectively.

## 4. Discussion

In this study, a CFD model that used a custom FSI coupling algorithm to simulate the fluid-driven motion of the BMHVs in the Realheart TAH has been developed and tested across a range of relevant operating conditions, highlighting the ability to extract applicable and important device results, and showing the robustness of the model to a change in these conditions.

The model used an overset modelling approach to both facilitate the valve motion and maintain a consistent and refined mesh on the surface of the leaflets and constant mesh quality throughout the flow domain. This yielded spatially well resolved wall shear stresses on the surface of the leaflets, highlighted in Figure 12.

The approach used to blend strong and weak coupling was a novel application of the two existing fluid flow and structural coupling algorithms, resulting in a new simulation method for artificial heart valves. Most artificial heart valve simulations have used strongly coupled approaches, as methods using solely weakly coupled schemes have had mixed success regarding

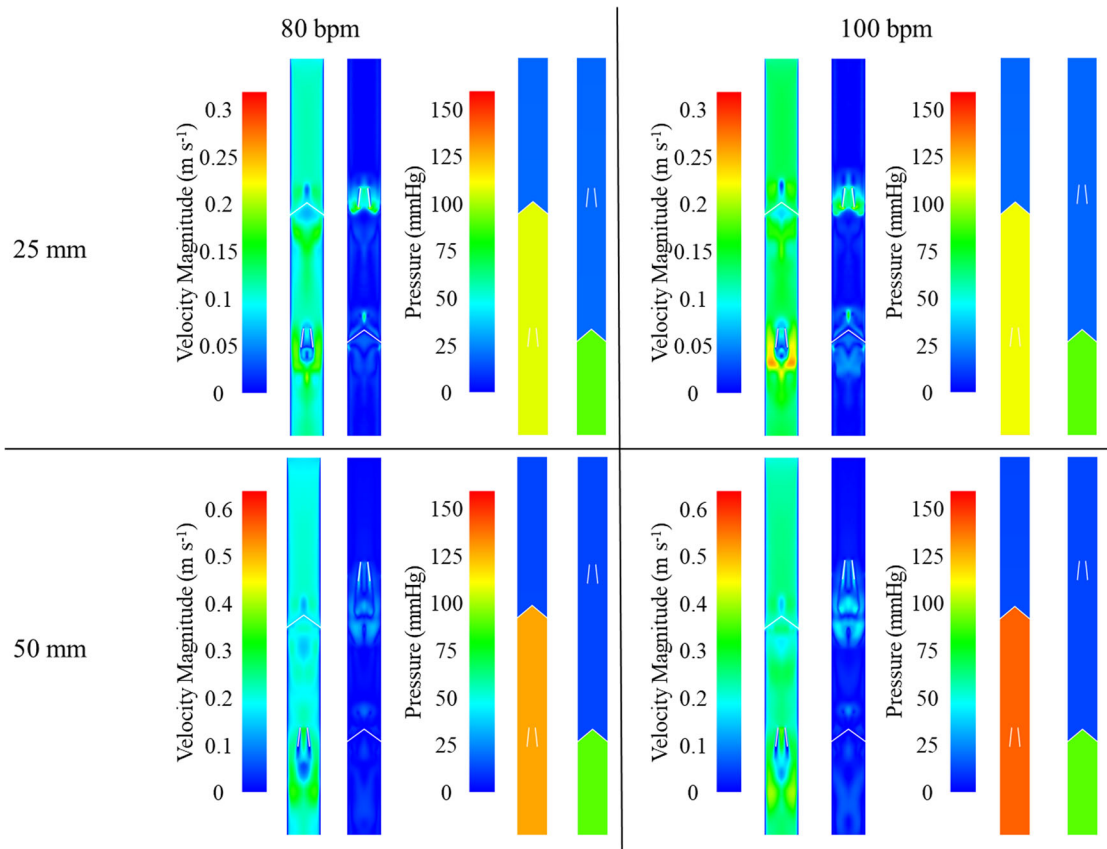


**Figure 7.** Velocity magnitude and pressure contours when leaflet angle is  $\theta = 44^\circ$  (fully open) for a change in stroke length and stroke rate. Note the scaling of the velocity magnitude contours is  $0\text{--}0.3\text{ m s}^{-1}$  for the 25 mm stroke length cases, and  $0\text{--}0.6\text{ m s}^{-1}$  for the 50 mm stroke length cases. Velocity magnitude contour plots are clipped to the maximum values of  $0.3\text{ m s}^{-1}$  and  $0.6\text{ m s}^{-1}$  in each of the cases respectively.

solution stability (Abbas et al. 2022). For this study, the blended weak-strong coupling and variable time stepping schemes were tuned to maximise computational efficiency whilst providing the minimum level of stability. Solution stability was established as solving until completion, rather than the solution diverging. The initial model used only weak coupling, and divergences in the solution arose at instantaneous valve opening - a problem also encountered by Borazjani et al. (2008). When strong coupling was introduced for small valve leaflet angles ( $<7^\circ$ ), stable solutions could be obtained. The threshold angle of  $7^\circ$  was the smallest threshold by which stability was maintained and maximised the computationally efficient portions of the cycle that were weakly coupled. Accuracy of the solution could be further improved by increasing the thresholds by which strong coupling was active, as was shown when comparing to a fully strongly coupled scheme and a second blended scheme with an additional threshold. B2 was included to capture leaflet rebound and fluttering, although this was not observed during the operating condition tested. B2 did however improve the accuracy of the solution whilst at a computational expense. Operating

conditions, particularly those found in a full TAH, may induce leaflet fluttering and rebound due to higher fluid velocities and subsequent fluid forces. Therefore, the second threshold may be required in these cases.

Using a variable time stepping scheme is common when simulating MHV motion when using the ALE method, as it limits mesh motion, and subsequent remeshing between time steps (Bang et al. 2006; Choi and Kim 2009; Annerel et al. 2012). For the OD method used in this study, limiting mesh motion leads to improved interpolation of data between the component meshes of the valve leaflets and the background mesh of the fluid cylinder - improving stability of the solution (Ansys 2021). In addition, by decreasing the time step size at valve opening and closing, the temporal resolution of the leaflet wall shear stress improved, which varied greatest during this time.

The accuracy of this specific solution could not be validated, as there was no physical representation of the simplified geometry to test against. However, the implementation of the method into the full Realheart TAH model, and experimental validation of that model, is the subject of future work. Historically, CFD

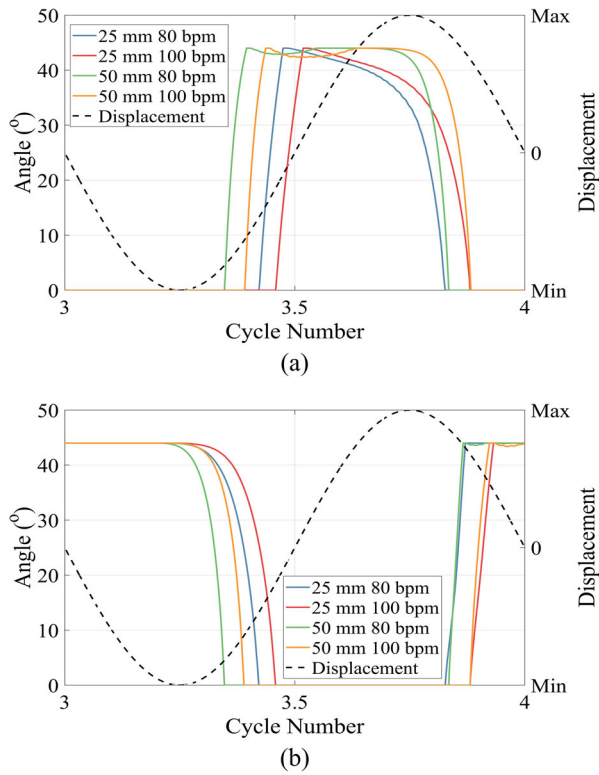


Figure 8. Valve motion over final cycle alongside AV plane displacement for the (a) mitral valve and (b) aortic valve.

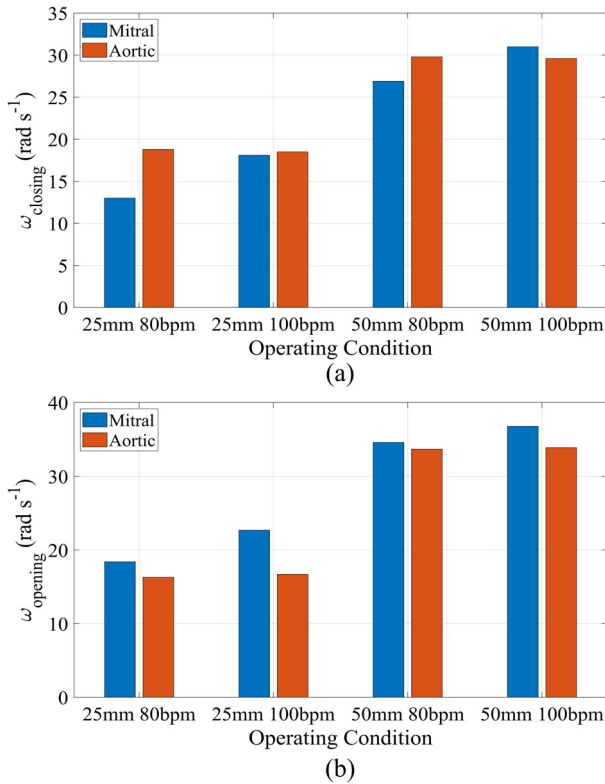


Figure 9. Change in (a)  $\omega_{closing}$  and (b)  $\omega_{opening}$  for the mitral and aortic valve leaflets with a change in stroke length and stroke rate.

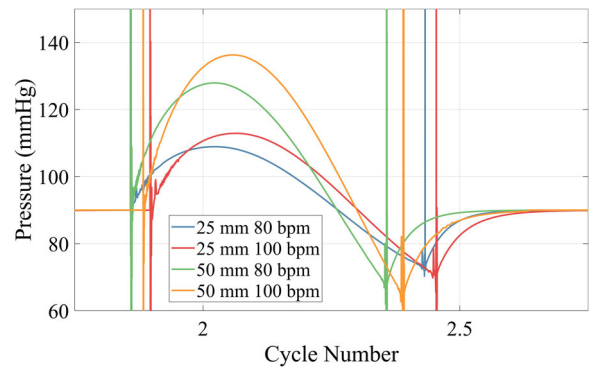


Figure 10. Variation in aortic pressure with a change in stroke length and stroke rate. Time frame limited between cycle number 1.75 and 2.75 to highlight variation during full range of aortic valve motion. Vertical lines correspond to instantaneous pressure spikes.

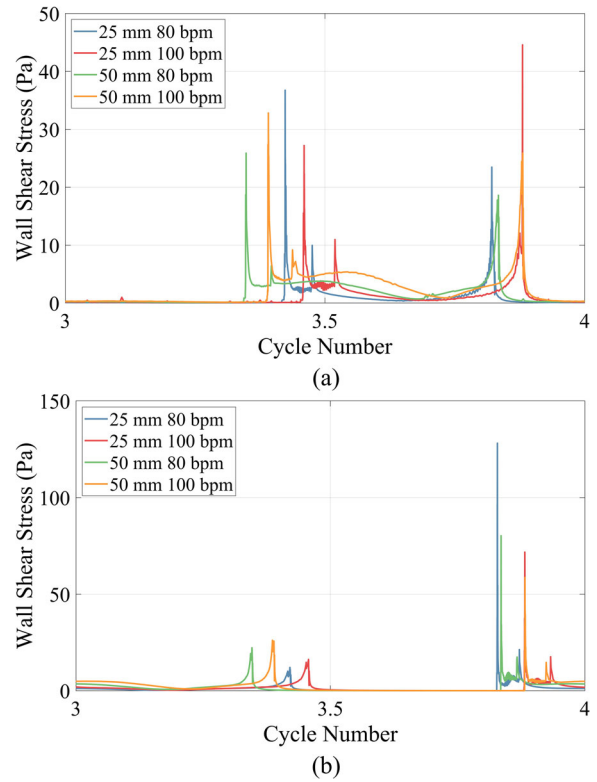
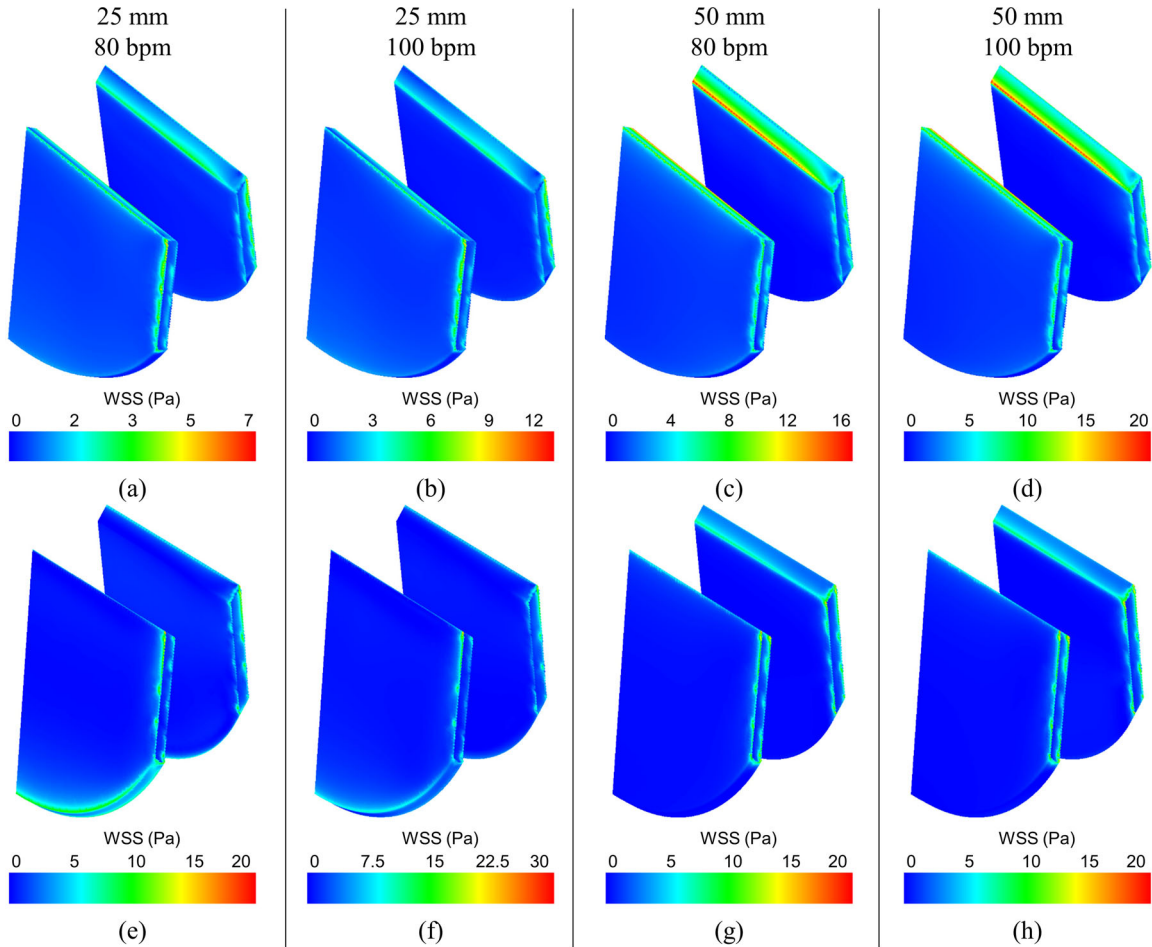


Figure 11. Variation in  $\overline{WSS}$  over the course of the last cycle for the (a) Mitral valve and (b) Aortic Valve.

studies on BMHVs have investigated valves that simply open and close, where the housing is fixed in position, which is the same as the function of the aortic valve in this study. The range of values of  $\omega_{opening}$  and  $\omega_{closing}$  for the aortic valve in this model (15 to 35 rad s<sup>-1</sup>) compares well against literature values of 11 to 50 rad s<sup>-1</sup> for  $\omega_{opening}$ , and 30 to 150 rad s<sup>-1</sup> for  $\omega_{closing}$  (Choi and Kim 2009; Borazjani et al. 2010; Su et al. 2015; Mirkhani et al. 2016), noting that these studies use different operating conditions to those used in this

**Table 3.**  $\overline{TAWSS}$  values for a variation in stroke length and stroke rate.

	25 mm/ 80 bpm	25 mm/ 100 bpm	50 mm/ 80 bpm	50 mm/ 100 bpm
$\overline{TAWSS}_{mitral}$	0.80	1.08	1.89	2.31
$\overline{TAWSS}_{aortic}$	1.16	1.50	1.98	2.32

**Figure 12.** Contour plot of wall shear values on surface of (a-d) aortic valve leaflet and (e-h) mitral valve leaflet when leaflet angle is  $\theta = 44^\circ$  (fully open), for a change in stroke length and stroke rate. Note a difference in scaling between individual contour images.

investigation. There are no studies that consider a vertical translation of a BMHV in addition to its opening and closing, and so the values for  $\omega$  cannot be compared directly to any of these studies, but it is noted that the values lie within the range of the literature for a stationary BMHV (10 to 40  $\text{rad s}^{-1}$  in this case).

There was a small rebound for both valves upon reaching fully open, a feature also observed by Borazjani et al. (2010). This feature was present in this model at 50 mm stroke length, but did not occur at the 25 mm cases, perhaps owing to the lower velocities and forces experienced at 25 mm compared to 50 mm. An increase in stroke rate and stroke length increased the translational velocity of the mitral valve, increasing fluid forces on the mitral valve leaflet, returning an increase in  $\omega_{closing}$  and  $\omega_{opening}$ . For the aortic valve, only an increase in stroke length brought about an increase in  $\omega_{closing}$  and

$\omega_{opening}$ , with the stroke rate changing very little. This may be attributed to the relatively small change in bulk fluid velocity between the 80 bpm and 100 bpm cases, as well as small variations in the cycle times in which the aortic valve opened and closed in each case.

The flow characteristics around the aortic valve were in line with what is normally observed, with the one central and two peripheral jet structures that correspond to the orifices when the valve is fully opened (Dasi et al. 2009), shown in Figure 7. The peripheral jets developed first and persisted for longer due to the fluid flowing around the outside of the opening valve leaflets. The central jet developed later, as upstream bulk fluid is pushed through the open valve by the closed mitral valve. When the mitral valve is fully open and moving upwards, the leaflets pierce through the stationary fluid in the valve's vicinity and create a

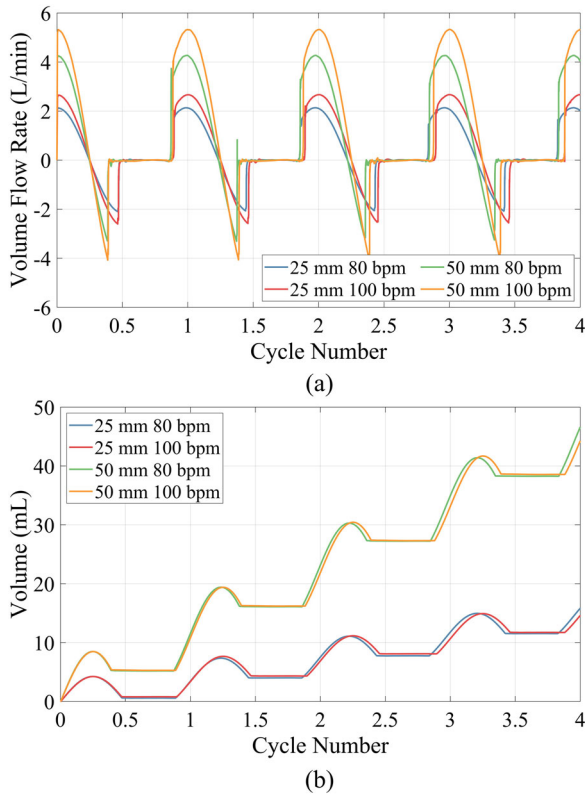


**Figure 13.** (a) Variation in  $Q_{inlet}$  for all four cycles with a variation in stroke length and stroke rate (b) Cumulative outlet flow over the four cycles.

trailing flow structure in its wake. At 25 mm stroke length, the wake is short and surrounds the surfaces of the valve leaflet. At 50 mm however, the valve moves much further upwards causing the wake to detach.

These flow features translate to wall shear on the surface of the valve leaflet. In Figure 12(a)–(d), the leading edge of the aortic valve experienced elevated shear stresses, as the central jet moved through the open valve. The level of shear stress increased with an increase in stroke length and stroke rate, as these parameters equated to an increase in peak fluid velocities past the valve. For the mitral valve in Figure 12(e)–(h), at 25 mm stroke length, the trailing edge experienced the elevated shear stresses due to the wake surrounding this area, whereas at 50 mm, this occurred on the leading edge as the valve moved upwards through stationary fluid. It was observed that an increase in stroke length and rate returned an increase in  $\overline{TAWSS}$  for both valves, attributed to the higher velocities caused by an increase in either of the two parameters.

The values of  $Q_{peak}$  increased for an increase in stroke rate and stroke length, as the value of  $Q$  at all times correlated directly with translational velocity of the mitral valve when it was closed.  $V_{backward}$  remained relatively consistent between cases, indicating that it is the volume

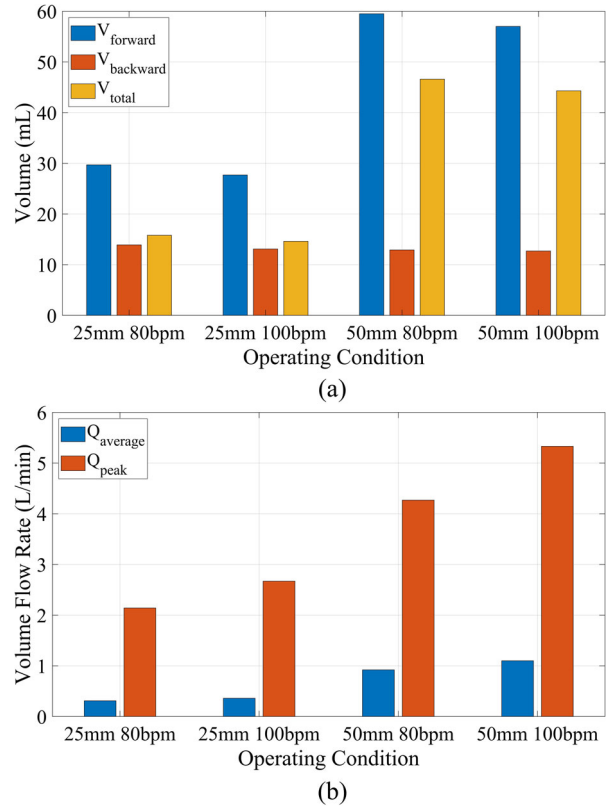


**Figure 14.** Variation in (a) volume flow and (b) volume flow rate through the outlet for a change in stroke length and stroke rate.

of fluid that moves back past the valve that determines its closure.

Pressures within the aorta varied as per the two-element Windkessel model that was applied at the outlet. The pressure variation followed the variation in  $Q_{outlet}$ , as the value of  $R$  in the Windkessel model was the driving force behind the change in pressure. The effect of the value of  $C$  can be seen at the ‘rebound’ pressure phase, where the aortic valve closes, and the pressure returns to the ambient pressure assigned to the Windkessel model – in this case 90 mmHg. The time taken for this rebound to return to ambient pressure was a function of the product of  $R$  and  $C$ . The inclusion of the two-element Windkessel model highlights the possibility for further lumped parameter or 1D representation of downstream, or indeed upstream, vasculature to obtain a more realistic physiological pressure response. For full device simulation, these parameters can easily be altered to represent real patient data, and the response of the device to that specific patient could be analysed.

#### 4.1. Limitations

In previous uses of overset meshing for evaluating artificial valve motion, authors have either chosen to

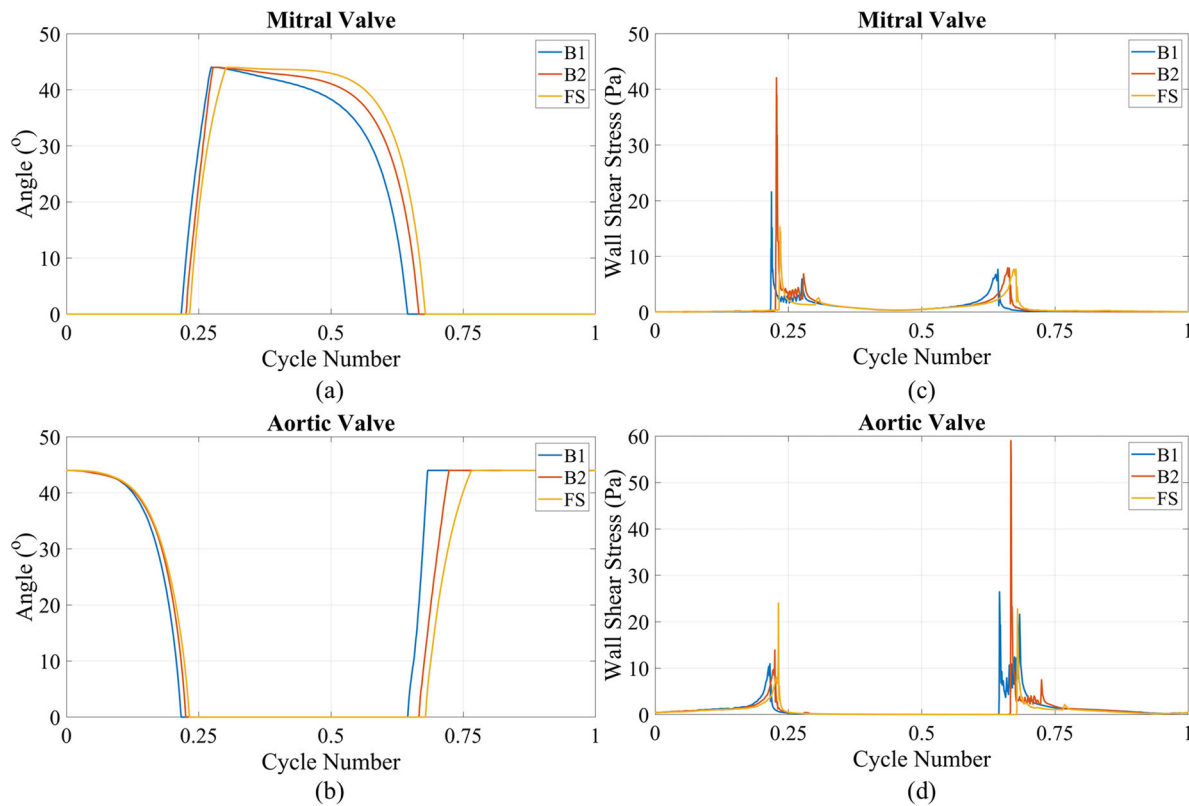


**Figure 15.** Comparison of blended scheme 1 (B1), blended scheme 2 (B2) and fully strongly coupled (FS) schemes for (a) mitral valve leaflet angle, (b) aortic valve leaflet angle, (c) mitral valve  $\overline{WSS}$  and (d) aortic valve  $\overline{WSS}$ .

include a *gap model* (Al-Azawy et al. 2016), where the cells in the gap between valve and valve housing are numerically ‘ignored’, or to explicitly model the gaps with a high-density region of cells (Nowak et al. 2020). In this study, there was no peripheral gap defined between the valve leaflet and valve housing, as a *gap model* was not available within the software, and a defined gap approach would have required approximately five times the number of elements, making model development challenging and time consuming. Peripheral gaps around the outside of mechanical heart valves do create high shear leakage flow, giving rise to the possibility of blood damage (Min Yun et al. 2014). Future studies where blood damage is the focus can include explicit gap modelling to account for this region.

The exclusion of a peripheral gap meant the fluid domain was divided into three separate closed sections at the point of either valve closing – the atrial, ventricle, and aortic regions. This is not a recommended approach, as the incompressibility of the fluid resulted in large pressure spikes during the period of instantaneous valve opening and closure, as seen in Figure 10 (Ansys 2021). These pressure transients did not affect the motion of the valves however, as the timeframe over which they occurred was very

small (<1ms), and the subsequent transient pressure became ‘smooth’ after the initial phase of valve opening. Future studies will seek to overcome these unrealistic pressure transients, either through the implementation of a *gap model* or a small amount of fluid compressibility.

The choice of stroke length and stroke rates considered in this study were the same as would be found within the Realheart TAH. However due to the smaller geometry of the fluid tube in this study, the flow rates that were produced were much smaller than that found in a clinical setting and produced flow profiles that were in the laminar range. Adding a turbulence model is straight forward however and could be included in future studies that consider flow regimes that are turbulent.

## 5. Conclusion

This study presented a new methodology for the motion of bileaflet heart valves, which we have demonstrated on a simple positive-displacement pump using such valves. The method used overset meshing to both enable the fluid-driven motion of the valve leaflets, as well as maintain a consistent and refined mesh around the leaflets. This resulted in efficient

capture of the valve leaflet kinematics across all ranges of motion, as well as high-quality wall shear stress capture on the surface of the leaflets. The proposed variable time-stepping scheme ensured computational efficiency, whilst improving the stability of the solution through the minimisation of mesh motion. The blended weak-strong coupling algorithm between the structural and fluid equations provided additional stability benefits, as it ensured only the most relevant range of motion required maximum computational stability, allowing for a more efficient computational approach for all other ranges of motion. This study demonstrated that the new methodology can be applied to the full range of physiologically relevant operating conditions, through the modification to the stroke length and stroke rate of the positive displacement mechanics. Velocity contours showed classical three jet flow features associated with bileaflet valves, angular velocities of the valves during opening and closing aligned with those found in the literature, and the variation in volume flow rate was typical of a pulsatile flow system. We have successfully identified a modelling approach that will allow for the efficient and accurate characterisation of full positive-displacement TAHs from both a haemodynamic and hemocompatibility perspective.

### Disclosure statement

AN and ILP are employees of, or consultants to, and/or shareholders of, Scandinavian Real Heart AB.

### Funding

JB PhD funded 50/50 from EPSRC and Scandinavian Real Heart AB (Reference: 2426107)

### References

Abbas SS, Nasif MS, Al-Waked R. 2022. State-of-the-art numerical fluid–structure interaction methods for aortic and mitral heart valves simulations: a review. *Simulation* (San Diego, Calif). 98(1):3–34.

Al-Azawy MG, Turan A, Revell A. 2016. An Overset mesh approach for valve closure: an LVAD application. p. 145–151.

Annerel S, Degroote J, Vierendeels J, Claessens T, Ransbeeck P V, Dahl SK, Skallerud Br, Hellevik LR, Segers P, Verdonck P. 2012. Application of a strong FSI coupling scheme for the numerical simulation of bileaflet mechanical heart valve dynamics: study of wall shear stress on the valve leaflets. *Progress in Computational Fluid Dynamics*. 12(2-3):68–79.

Ansys, Inc. 2021. *Ansys Fluent: User Guide* (Version 2021 R1) [Computer software], Ansys, Inc.

Bang JS, Yoo SM, Kim CN. 2006. Characteristics of pulsatile blood flow through the curved bileaflet mechanical heart valve installed in two different types of blood vessels: velocity and pressure of blood flow. *ASAIO j.* 52(3): 234–242.

Bavo AM, Rocatello G, Iannaccone F, Degroote J, Vierendeels J, Segers P. 2016. Fluid-structure interaction simulation of prosthetic aortic valves: comparison between immersed boundary and arbitrary Lagrangian-Eulerian techniques for the mesh representation. *PLoS One*. 11(4):e0154517.

Borazjani I. 2013. Fluid–structure interaction, immersed boundary-finite element method simulations of bio-prosthetic heart valves. *Comput Methods Appl Mech Eng*. 257: 103–116.

Borazjani I, Ge L, Sotiropoulos F. 2008. Curvilinear immersed boundary method for simulating fluid structure interaction with complex 3D rigid bodies. *J Comput Phys*. 227(16):7587–7620.

Borazjani I, Ge L, Sotiropoulos F. 2010. High-resolution fluid–structure interaction simulations of flow through a bi-leaflet mechanical heart valve in an anatomic aorta. *Ann Biomed Eng*. 38(2):326–344.

Carlsson M, Ugander M, Mosen H, Buhre T, Arheden H. 2007. Atrioventricular plane displacement is the major contributor to left ventricular pumping in healthy adults, athletes, and patients with dilated cardiomyopathy. *Am J Physiol - Heart Circ Physiol*. 292(3):1452–1459.

Choi CR, Kim CN. 2009. Numerical analysis on the hemodynamics and leaflet dynamics in a bileaflet mechanical heart valve using a fluid-structure interaction method. *Asaio J.* 55(5):428–437.

Darbyshire AG, Mullin T. 1995. Transition to turbulence in constant-mass-flux pipe flow. *J Fluid Mech*. 289:83–114.

Dasi LP, Simon HA, Sucusky P, Yoganathan AP. 2009. Fluid mechanics of artificial heart valves. *Clin Exp Pharmacol Physiol*. 36(2):225–237.

Dumont K, Stijnen JMA, Vierendeels J, van de Vosse FN, Verdonck PR. 2004. Validation of a fluid-structure interaction model of a heart valve using the dynamic mesh method in fluent. *Comput Methods Biomech Biomed Engin*. 7(3):139–146.

Ge L, Jones SC, Sotiropoulos F, Healy TM, Yoganathan AP. 2003. Numerical simulation of flow in mechanical heart valves: grid resolution and the assumption of flow symmetry. *J Biomech Eng*. 125(5):709–718.

Gilmanov A, Le TB, Sotiropoulos F. 2015. A numerical approach for simulating fluid structure interaction of flexible thin shells undergoing arbitrarily large deformations in complex domains. *Comput Phys*. 300(C):814–843.

Gilmanov A, Sotiropoulos F. 2016. Comparative hemodynamics in an aorta with bicuspid and trileaflet valves. *Theor Comput Fluid Dyn*. 30(1-2):67–85.

Han JJ. 2021. Aeson—The Carmat total artificial heart is approved for enrollment in the United States. *Artif Organs*. 45(5):445–446.

Spühler JH, Hoffman J. 2021. An interface-tracking unified continuum model for fluid-structure interaction with topology change and full-friction contact with application to aortic valves. *Int J Numer Methods Eng*. 122(19): 5258–5278.

- Hsu M-C, Kamensky D, Xu F, Kiendl J, Wang C, Wu MCH, Mineroff J, Reali A, Bazilevs Y, Sacks MS. 2015. Dynamic and fluid–structure interaction simulations of bioprosthetic heart valves using parametric design with T-splines and Fung-type material models. *Comput Mech.* 55(6):1211–1225.
- Kelly NS, McCree D, Fresiello L, Brynedal Ignell N, Cookson AN, Najjar A, Perkins IL, Fraser KH. 2022. Video-based valve motion combined with computational fluid dynamics gives stable and accurate simulations of blood flow in the Realheart total artificial heart. *Artif Organs.* 46(1):57–70.
- Kolahdouz EM, Bhalla APS, Scotten LN, Craven BA, Griffith BE. 2021. A sharp interface Lagrangian-Eulerian method for rigid-body fluid-structure interaction. *Comput Phys.* 443:110442.
- Lippi G, Sanchis-Gomar F. 2020. Global epidemiology and future trends of heart failure. *AME Med J.* 5:15–15.
- Luraghi G, Wu W, De Castilla H, Rodriguez Matas JF, Dubini G, Dubuis P, Grimmé M, Migliavacca F. 2018. Numerical approach to study the behavior of an artificial ventricle: fluid–structure interaction followed by fluid dynamics with moving boundaries. *Artif Organs.* 42(10):E315–E324.
- Melton N, Soleimani B, Dowling R. 2019. Current role of the total artificial heart in the management of advanced heart failure. *Curr Cardiol Rep.* 21(11):1–7.
- Min Yun B, Aidun CK, Yoganathan AP. 2014. Blood damage through a bileaflet mechanical heart valve: a quantitative computational study using a multiscale suspension flow solver. *J Biomech Eng.* 136(10):101009–101009.
- Mirkhani N, Davoudi MR, Hanafizadeh P, Javidi D, Saffarian N. 2016. On-X heart valve prosthesis: numerical simulation of hemodynamic performance in accelerating systole. *Cardiovasc Eng Technol.* 7(3):223–237.
- Mohacsi P, Leprince P. 2014. The CARMAT total artificial heart. *Eur J Cardiothorac Surg.* 46(6):933–934.
- Nestola MGC, Becsek B, Zolfaghari H, Zulian P, De Marinis D, Krause R, Obrist D. 2019. An immersed boundary method for fluid-structure interaction based on variational transfer. *Comput Phys.* 398:108884.
- NHSBaT. 2021. Organ donation and transplant activity report 2020/21. NHS Blood and Transplant.
- Nobili M, Morbiducci U, Ponzini R, Del Gaudio C, Balducci A, Grigioni M, Maria Montevicchi F, Redaelli A. 2008. Numerical simulation of the dynamics of a bileaflet prosthetic heart valve using a fluid–structure interaction approach. *J Biomech.* 41(11):2539–2550.
- Nowak M, Adamczyk W, Melka B, Ostrowski Z, Bialecki R. 2020. Numerical model of the aortic valve implanted within real human aorta. Cham: Springer International Publishing; p. 265–275.
- Slepian MJ, Alemu Y, Girdhar G, Soares JS, Smith RG, Einav S, Bluestein D. 2013. The Syncardia™ total artificial heart: in vivo, in vitro, and computational modeling studies. *J Biomech.* 46(2):266–275.
- Su B, Kabinejadian F, Phang HQ, Kumar GP, Cui F, Kim S, Tan RS, Hon JKF, Allen JC, Leo HL, et al. 2015. Numerical modeling of intraventricular flow during diastole after implantation of BMHV. *PLoS One.* 10(5):e0126315.
- Szabo Z, Holm J, Najjar A, Hellers G, Pieper IL, Casimir Ahn H. 2018. Scandinavian real heart (SRH) 11 implantation as total artificial heart (TAH)-experimental update. *J Clin Exp Cardiol.* 09(03):1–4.
- Tian F-B, Dai H, Luo H, Doyle JF, Rousseau B. 2014. Fluid–structure interaction involving large deformations: 3D simulations and applications to biological systems. *Comput Phys.* 258:451–469.
- Torregrossa G, Morshuis M, Varghese R, Hosseinian L, Vida V, Tarzia V, Loforte A, Duveau D, Arabia F, Leprince P, et al. 2014. Results with syncardia total artificial heart beyond 1 year. *ASAIO J.* 60(6):626–634.